Materials Advances

ROYAL SOCIETY OF CHEMISTRY

PAPER

View Article Online
View Journal | View Issue

Cite this: *Mater. Adv.*, 2024, 5, 2271

Morphology-controlled synthesis of a NiCo-carbonate layered double hydroxide as an electrode material for solid-state asymmetric supercapacitors†

Sudhir Kumar, Biraj Kanta Satpathy and Debabrata Pradhan *

Transition metal carbonate hydroxides are emerging as potential candidates as electrode materials for efficient energy storage systems. Herein, we report the solvothermal synthesis of NiCo-layered double hydroxide carbonate hybrid or NiCo–carbonate layered double hydroxide (NiCo–CH) nanostructures as active electrode materials for energy storage in supercapacitors. The morphology and physicochemical properties of the NiCo–CH nanostructure are tailored by controlling the synthesis parameters. The NiCo–CH nanorods synthesized at 180 °C (NiCo–CH-180) deliver the best performance, *i.e.*, a specific capacitance of 762 F g^{-1} at 1 A g^{-1} current density, among the as-synthesized NiCo–CHs. An asymmetric supercapacitor (ASC) device fabricated using NiCo–CH-180 as the positive electrode and activated carbon (AC) as the negative electrode (NiCo–CH-180//AC) exhibits an energy density of 52 W h kg^{-1} with a power density of 1500 W kg^{-1} at 2 A g^{-1} current density. The fabricated ASC retains 76.2% of its capacitance after 5000 charge–discharge cycles, which corroborates its good cycling stability. This work demonstrates an effective strategy to synthesize a well-defined NiCo–CH nanostructure as an electrode material for energy storage applications.

Received 15th November 2023,
Accepted 27th January 2024

DOI: 10.1039/d3ma01008b

rsc.li/materials-advances

1. Introduction

The excessive demand and consumption of non-renewable energy resources such as coal, oil, and natural gas endangers human survival because of the detrimental ecological environment and changing global climates.[1] Thus the development and use of environmentally acceptable renewable energy resources to combat global warming and pollution are highly desirable. The solar, hydro, wind, and other renewable energy sources have considerably reduced extreme power and environmental challenges over the last decade.[2–4] The power generated from solar, hydro, and wind resources needs to be efficiently stored for use whenever required.[5] Thus, attention has been paid recently to exploring sustainable and efficient energy storage systems to address the future energy demand for emerging technologies.[6] Developing an energy storage system with appropriate power density and energy density, as well as longer cycle life, is the main challenge to maximize the use of portable electronic devices.[7,8] Fuel cells, ion batteries, and supercapacitors are the major energy storage devices that play important roles for future generation electronic devices.[9,10] Among the energy storage devices, supercapacitors (electrochemical capacitors) have the potential to overcome the existing challenges, such as the use of noble-metal-based electrocatalysts for fuel cells, and the poor cycling stability, safety issues, and limited Li-reserves for ion-batteries. The fast-charging capability, comparatively low to moderate energy density, and moderate to high power density have advantageous properties for supercapacitors with a major limitation of relatively low energy density. Supercapacitors are categorized into two types based on charge/ion storage mechanisms, one is electric double-layer capacitors (EDLCs) and the other is pseudocapacitors (PCs). In EDLCs, the charges are stored on the electrode surface through the formation of an electric double layer. In PCs, the charge storage occurs through faradaic reactions, intercalation, and diffusion processes that take place on the electrode surface.[11] A combination of both mechanisms is termed a hybrid supercapacitor.[8]

The electrode materials play a significant role in an efficient supercapacitor device with high energy and power density. Carbon-based materials such as porous carbon, graphene, carbon fibers, carbon nanotubes, carbon foam, and activated carbon show EDLC behavior. The specific capacitances of the carbon-based electrode materials can be achieved up to 250 F g^{-1} because of their high specific surface area.[12] On the other hand, the

Materials Science Centre, Indian Institute of Technology, Kharagpur 721 302, WB, India. E-mail: deb@matsc.iitkgp.ac.in

† Electronic supplementary information (ESI) available. See DOI: https://doi.org/10.1039/d3ma01008b

transition metal oxides (NiO, MnO_2, Co_3O_4),[13–15] hydroxides ($Co(OH)_2$@$Cu(OH)_2$),[16] carbonates ($NiCo(CO_3)(OH)_2$),[17] chalcogenides,[18] and conductive polymers (PANI, PPy)[19,20] are found to show PC behavior. Although the specific capacitance and energy density are higher for PCs, their cycling stability remains lower than that of EDLCs because of the faradaic redox reaction. To increase the electrochemical performance, designing PCs using suitable electrode materials is expected to increase the energy storage performance. The one-dimensional (1D) and two-dimensional (2D) nanomaterials have been reported to store more charges and exhibit higher electrochemical performance because of their large surface area and provide a shorter distance for charge transportation.[21,22]

Bimetallic carbonate hydroxide (CH) is an emerging material that has multiple metal oxidation states and redox reaction activity. It has received significant attention as an electrode material for the oxygen evolution reaction[23] and for supercapacitor applications.[24] The inorganic lamellar structure of bimetallic hydroxide anions has a typical formula of $[M_{2-x}^{2+}M_x^{3+}(OH)_{4-n}A^{n-}]\cdot mH_2O$, where M^{2+} are bivalent, M^{3+} are trivalent metal cations and A^{n-} are anions (*e.g.*, CO_3^{2-}, NO_3^{2-}, Br^-).[25] These layered double hydroxides have been found to show new functionalities and structures that influence the valence state and thereby increase the electrochemically active sites and wettability.[26–28] Moreover, the inter-planar spacing of the layered structure allows easy diffusion of the ions to improve the electrochemical and charge storage performance.[29–31] Several forms of transition metal oxide/hydroxide/carbonate and their composites have recently been investigated for their electrochemical applications, including supercapacitors. The NiCo–CH has been identified as a viable material as a positive electrode material because of its natural abundance, high theoretical specific capacitance, environmental friendliness, and higher number of active sites.[17,32] As an example, Bastakoti *et al.* reported a NiCo–$(OH)_2$@NiCo–$(CO_3)(OH)_2$ electrode material that shows 632 F g^{-1} of specific capacitance at a 5 mV s^{-1} scan rate.[33] Subsequently, there are several studies on NiCo-based carbonate hydroxides as electrode materials for supercapacitor applications.[34–38] In these studies, efforts are made to optimize the size, morphology, and composition (Ni : Co ratio) for an enhanced energy storage performance. Zhang *et al.* synthesized $Co(CO_3)_{0.5}(OH)$/$Ni_2(CO_3)(OH)_2$ with different morphologies (nanosheets, nanobelts, and nanorods) using a two step process by varying the amount of ammonia.[36] The ammonia amount in the precursor solution played an important role in controlling the size, morphology, and composition of $Co(CO_3)_{0.5}(OH)$/$Ni_2(CO_3)(OH)_2$, which in turn showed different electrochemical performances. With 3 mL ammonia in the precursor solution, nanobelts are formed which show the best electrochemical storage performance of 987 F g^{-1} at 1 A g^{-1}.[36] Recently, modifications on NiCo- and other LDHs have been performed to further enhance the supercapacitor performance.[39–41] It is revealed that the best supercapacitor performance in NiCo–CH is primarily due to the optimized morphology and Ni : Co ratio.[42] Recently, Bhatt *et al.* reported that the Ni : Co ratio leads to a change in the electronic properties of the material and thus the electrochemical performance.[43] In particular, oxygen vacancies are found as the main defects in NiCo–CH that are preferred at Ni sites. The active sites are also correlated to the surface morphology in the electrode material, which plays a crucial role in electrochemical performance.

In this article, we demonstrate the synthesis of a NiCo-carbonate layered double hydroxide using a solvothermal method by varying the principal parameters, such as growth temperature, Ni/Co-precursor ratio, synthesis duration and reaction medium, as well as the role of the surfactant for the formation of diverse morphologies (nanorod, microcube, microplate and urchin-like). Although there is literature on NiCo-carbonate layered double hydroxides of different morphologies, they were reported separately.[34–36,39] One of the novelties of the current work is to demonstrate different NiCo–CH morphologies in a single-step process by varying the experimental parameters. The varied experimental parameters lead to a change in not only the morphology but also the Ni : Co ratio, which has a significant role in the electrochemical performance. Synthesizing desirable morphology and structure is a challenging and crucial task to maximize the electrochemically active surface. To our knowledge, a systematic synthesis and controlled morphology study of NiCo–CHs using a solvothermal method by varying the reaction parameters have not yet been reported. The synthesized materials in the present work are studied for their electrochemical properties and we demonstrate their performance for supercapacitor applications. The specific capacitance of 762 F g^{-1} is achieved for the sample NiCo–CH-180 (prepared at 180 °C) at 1 A g^{-1} current density. The asymmetric supercapacitor (ASC) using NiCo–CH-180 and activated carbon as the positive and negative electrode material, respectively, delivers a maximum energy density of 52 W h kg^{-1} and power density of 1500 W kg^{-1}. Moreover, the same device retains more than 75% capacitance after 5000 charge–discharge cycles, revealing good cycling stability.

2. Materials and methods

2.1 Materials

The main raw materials used in this work, including nickel(II) nitrate hexahydrate [$Ni(NO_3)_2\cdot6H_2O$], cobalt(II) nitrate hexahydrate [$Co(NO_3)_2\cdot6H_2O$], ethylene glycol (EG) [$C_2H_6O_2$], urea (H_2NCONH_2), cetyltrimethylammonium bromide (CTAB) [$C_{19}H_{42}BrN$], potassium hydroxide (KOH), polyvinyldifloride (PVDF) [–($C_2H_2F_2$)–], activated carbon (AC) and *N*-methylenepyrolidine (NMP) [C_5H_9NO], and all other chemicals were purchased from Merck (Mumbai, India). All of above the mentioned chemicals are analytical grade and used without any further purification.

2.2 Synthesis of NiCo–CH

In a typical synthesis process, metal salt precursors, CTAB, and urea were added to a mixed solvent (15 mL EG + 20 mL water) and the preceding solution was transferred to an autoclave for solvothermal treatment. The metal salt precursors, *i.e.*, nickel

nitrate and cobalt nitrate with selected amounts (molar ratio of 2 : 1, 1 : 1, and 1 : 2) were added to the mixed solvent. Then fixed amounts of cetyltrimethylammonium bromide (CTAB) (0.5 g) and urea (0.9 g, *i.e.*, 15 mmol) were added and stirred for 30 min. The homogeneous solution was then transferred into a Teflon-lined stainless-steel autoclave. The autoclave was kept in a muffle furnace at a selected temperature (120 to 200 °C) for a specific duration (12 h) for the solvothermal reaction. After the completion of the reaction, the furnace was naturally cooled and the formed products were washed with isopropanol and water and then finally dried at 60 °C for 18 h. The obtained products are assigned as NiCo–CH-120, NiCo–CH-140, NiCo–CH-160, NiCo–CH-180 and NiCo–CH-200, and were synthesized at reaction temperatures of 120, 140, 160, 180 and 200 °C, respectively, with other reaction parameters fixed. The reactions were further performed with only a single solvent, *i.e.*, either EG [NiCo–CH-180(EG)] or water [NiCo–CH-180(H_2O)] to find the effect of the solvent medium with a fixed 2 : 1 Ni : Co ratio and at 180 °C. The effect of the surfactant (*i.e.*, CTAB) was studied with and without it using a 2 : 1 Ni : Co ratio and at 180 °C. Furthermore, the solvothermal reaction duration was varied from 6 to 72 h to find its effect on the product while keeping other parameters fixed. The detailed experimental parameters by varying the precursor concentration, solvent, reaction temperature, and duration are presented in Table S1, ESI.†

2.3 Material characterization

The crystal structure and phase analysis of the as-synthesized materials were carried out by powder X-ray diffraction (Malvern Panalytical-Empyrean diffractometer) operated at 40 mA and 45 kV for a 2θ scan using Ni-filtered Cu K_α X-ray radiation in reflection geometry, equipped with a position sensitive detector. Chemical bond stretching, vibration, and functional groups were recorded with Fourier Transform Infrared (FTIR-Spectrophotometer, NICOLET 6700). The surface elemental and atomic oxidation states of a selective sample were analyzed by using X-ray photoelectron spectroscopy (XPS, PHI 500 Versa Probe II) with a monochromatic Al Kα X-ray source (1486.6 eV). The surface morphology of all the prepared materials was examined using a field emission scanning electron microscope (FESEM, Gemini 500, Zeiss). The elemental composition of the synthesized samples was measured by energy dispersive X-ray spectroscopy (EDS) analysis using an EDAX detector attached to the FESEM. The microstructure and lattice information were obtained using a transmission electron microscope (TEM, JEOL JEM-2100). The surface area and pore size were estimated by Brunauer–Emmett–Teller (BET) analysis with an autosorb iQ_2 volumetric physisorption analyzer (Quantachrome, ChemBET analyzer) using N_2 adsorption–desorption isotherms at 77 K.

2.4 Electrochemical measurements

The electrochemical study of all the synthesized materials was performed in a three-electrode configuration with a saturated calomel electrode (SCE), graphite rod, and fabricated electrode as the reference, counter, and working electrode, respectively.

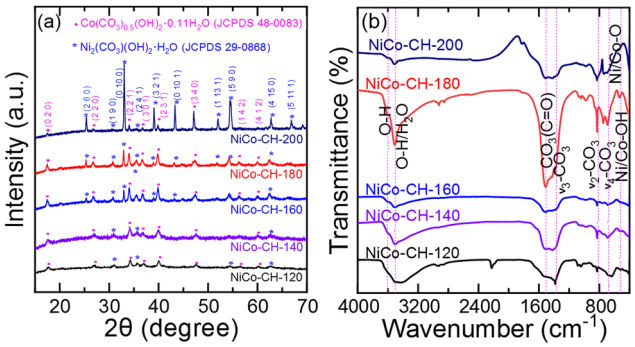

Fig. 1 (a) XRD patterns and (b) FTIR spectra of NiCo–CH prepared at different solvothermal temperatures (120, 140, 160, 180, and 200 °C) while keeping other synthesis parameters fixed, *i.e.*, 2 : 1 Ni : Co precursor, 15 mL EG + 20 mL water solvent, and 12 h.

The energy storage capability of the synthesized materials was measured from cyclic voltammetry (CV), galvanostatic charge–discharge (GCD), and electrochemical impedance spectroscopy (EIS) techniques using a CHI 760D electrochemical workstation (CH Instruments, Inc., USA). For electrode fabrication, the synthesized NiCo–CH, activated carbon (AC), and PVDF were taken in the weight ratio of 70 : 20 : 10 and ground in a mortar-pestle to form a homogeneous slurry with NMP as a solvent. The homogeneous slurry was coated on the clean 1 × 1 cm^2 Ni-foam with 1 mg loading of active material (NiCo–CH) and dried at 60 °C overnight. The Ni-foam was cleaned with 3 M HCl, isopropanol, and Millipore water for 10 min sonication for each and then dried. In the electrode fabrication, AC was used as a conductive matrix, PVDF as a binder, and Ni-foam as a current collector. All electrochemical measurements were performed in 2 M KOH electrolyte.

2.5 PVA-KOH gel synthesis

To prepare the PVA + KOH polymeric electrolyte gel, 1.0 g of PVA was poured into 10 mL of Millipore water in a 50 mL beaker and placed on a magnetic stirrer hot plate at 80 °C for three hours. Then 1.12 g of KOH (2 M) was added in 10 mL of Millipore water. The preceding solutions were mixed under stirring at 80 °C until the solution became a transparent gel.

3. Results and discussion

3.1 Crystal structure

The obtained XRD patterns (Fig. 1(a)) are analyzed to confirm the formation of nickel cobalt carbonate hydroxide and its crystal phase structure. The diffraction peaks are indexed to the orthorhombic crystal structure of nickel carbonate hydroxide as per JCPDS no. 29-0868[44] and cobalt carbonate hydroxide hydrate as per JCPDS no. 48-0083.[45] The products obtained at different reaction temperatures produce the same orthorhombic crystal structure for nickel and cobalt carbonate hydroxide. The cobalt carbonate hydroxide phase predominates at lower growth temperature (120 and 140 °C). At a higher solvothermal reaction temperature (160 to 200 °C), the increased diffraction

intensity indicates dominance in the formation of crystalline nickel carbonate hydroxide. This result implies the crystalline phase dominance at a higher solvothermal synthesis temperature.[37] The formation of the crystalline cobalt carbonate hydroxide phase at low temperatures as compared to nickel carbonate hydroxides can be attributed to differences in the thermodynamic properties of the respective compounds under the given synthesis conditions.[46] The thermodynamic stability of a compound is governed by its Gibbs free energy of formation. The Gibbs free energy of Co^{2+} is known to be more negative, resulting in easier formation of a cobalt complex than a nickel complex.[47] The Raman spectra of the synthesized NiCo–CHs with varying solvothermal temperatures (120–200 °C) are collected (Fig. S1, ESI†). The sample prepared at a low synthesis temperature (120 °C) shows absence in distinct Raman features. The samples prepared at 140 and 160 °C show two broad bands at ~523 cm^{-1} and ~1090 cm^{-1} corresponding to the Ni/Co–OH lattice vibration[48] and symmetric stretching vibration of the CO_3^{2-} group.[49] On the other hand, the samples prepared at higher synthesis temperature (180 and 200 °C) show a single intense peak at ~1090 cm^{-1} indicating an enhanced crystalline structure resulting from the ordering of the carbonate ions.[50] The observed variations in the Raman spectra characteristics of the NiCo–CH synthesized at different temperatures can be ascribed to several influencing factors, encompassing crystal structure and composition, which depends on the synthesis temperature. In particular, the Ni : Co ratio is higher at higher synthesis temperature (discussed later) and predominant formation of Ni carbonate is confirmed from the XRD. This leads to a strong Raman signal. The improved crystallinity is also confirmed from the sharp and intense diffraction peaks, which is observed in the XRD pattern for the sample synthesized at higher temperature. The FTIR spectra of the NiCo–CH, synthesized at different solvothermal temperatures are shown in Fig. 1(b). The broad feature at 3600–3510 cm^{-1} is due to the stretching vibration of the hydroxyl group. The peaks at ~1517 and 1396 cm^{-1} are attributed to the CO_3^{2-} asymmetric stretching mode (ν_3). The peak at ~830 cm^{-1} is due to the bending mode (ν_2) of the $(CO_3)^{2-}$ units. The peaks at 680 and 750 cm^{-1} are due to the bending mode (ν_4) of the $(CO_3)^{2-}$ units.[51] The carbonate ions in the Co and Ni structure are linked to the weak bands centered around 950 (ν_2) and 1040 cm^{-1} (ν_1), respectively. The stretching vibrations of the Ni–O/Co–O and Ni/Co–OH bands are ascribed at 536 and below 500 cm^{-1}, respectively.[52] This demonstrates the presence of functional groups such as carbonate and hydroxide in the synthesized samples.

3.2 Morphology

3.2.1 Effect of solvothermal temperature. The FESEM images of the NiCo–CHs, synthesized at different reaction temperatures with a 2 : 1 molar ratio of Ni : Co precursor, are shown in Fig. 2(a)–(e). The 1D nanostructure is obtained in the solvothermal reaction temperature range of 120–180 °C, whereas the 2D structure at 200 °C. At low synthesis temperatures (120 and 140 °C), the 1D feature appears as a bundle of nanowires indicating their agglomeration. The diameter and length of the nanowires are measured to be in the range of 15–20 and 200–500 nm, respectively. At moderate temperatures (160 and 180 °C), the 1D features are distinct and individual entities in the shape of nanorods. Moreover, the diameter of the 1D structure (nanorods) is found to be increased to 25–30 nm as compared to nanowires obtained at lower temperatures. At high solvothermal temperature (200 °C), the obtained product is found to be in the shape of microplates.

3.2.2 Effect of Ni and Co precursor concentration. Three different molar ratios of Ni : Co are taken for the synthesis of NiCo–CH at 180 °C while keeping other parameters fixed, *i.e.*, mixed solvent (15 mL EG + 20 mL water), 0.5 g CTAB, 15 mg urea, and 12 h reaction duration. With Ni : Co molar salt precursor concentrations ratio of 1 : 2, 1 : 1, and 2 : 1, the obtained products show microcube, urchin, and nanorod morphology, respectively (Fig. S2, ESI†). The morphology analysis reveals that higher nickel concentration leads to a nanorod morphology.

3.2.3 Effect of solvent. In previous cases, a mixed solvent (15 mL EG and 20 mL water) was used to obtain nanowires, nanorods, microcubes, and microplates. It is to be noted that neither only EG nor water produced a distinct morphology. In particular, agglomerated structures (Fig. S3a, ESI†) composed of nanoparticles and a few short nanorods are obtained by using only water as a solvent. On the other hand, nanoparticles (Fig. S3b, ESI†) are obtained with only EG as a solvent.

3.2.4 Effect of solvothermal duration. The reaction duration plays an important role in the shape and size of the nanostructures. To study the effect of reaction duration, solvothermal reaction was conducted from 6 to 72 h with other parameters fixed (180 °C, 2 : 1 Ni : Co, and 15 mL EG + 20 mL water solvent). With a short reaction duration of 6 h [NiCo–CH-180 (6 h)], nanorod-like features (Fig. S4a, ESI†) are found with short length (<250 nm). With a reaction duration of 12 h [NiCo–CH-180 (12 h)], well-defined nanorods of length ~350 nm are found (Fig. S4b, ESI†). After the 18 h reaction [NiCo–CH-180 (18 h)], the length and diameter are again increased to ~400 nm and ~40 nm, respectively (Fig. S4c, ESI†). Upon further increasing the reaction duration to 24 h, the obtained product [NiCo–CH-180 (24 h)] exhibits a reduction in the length and diameter of the nanorods (Fig. S4d, ESI†) indicating the dissolution of the product. After 48 h of synthesis duration, the obtained sample [NiCo–CH-180 (48 h)] shows agglomerated nanorods along with rectangular shaped microplates (Fig. S4e, ESI†), indicating the emergence or evolution of a new morphology. With a further increase in the reaction duration to 72 h, rectangular-shaped microplate growth is predominant for NiCo–CH-180 (72 h) as observed in the FESEM image (Fig. S4f, ESI†). The morphology study reveals the formation of nanorods initially, followed by the establishment of a well-defined nanorod structure up to 18 h, and then dissolution occurred, with final morphology evolution to rectangular microplates. These results suggest that the solvothermal synthesis duration plays a crucial role in tailoring the morphology of the NiCo–CH product.

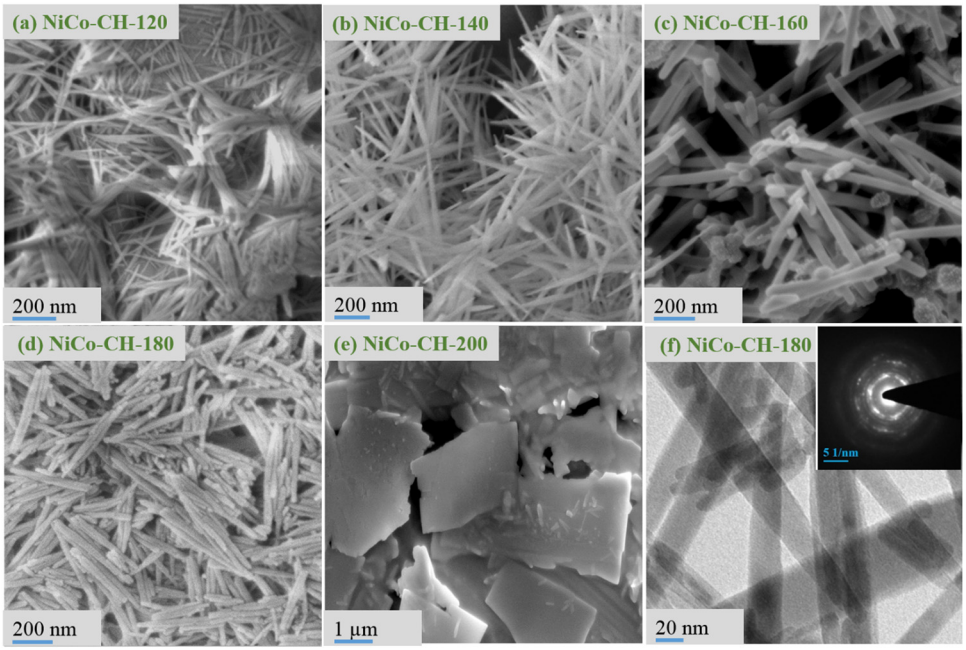

Fig. 2 FESEM images of NiCo–CH synthesized at a solvothermal temperature of (a) 120 °C, (b) 140 °C, (c) 160 °C, (d) 180 °C, and (e) 200 °C while other parameters are fixed (2 : 1 Ni : Co precursor, 15 mL EG + 20 mL water, 12 h). (f) TEM image of the sample NiCo–CH-180 obtained at 180 °C and the inset shows the SAED pattern of the corresponding sample.

3.2.5 Effect of surfactant. The surfactant plays a role in the morphology of the NiCo–CH. In the initial synthesis experiment, urchin-like structures of NiCo–CH (Fig. S5a and b, ESI†) are obtained without a surfactant. The urchin structure composed of nanowires exhibits lower supercapacitance behaviour and thus subsequent experiments were carried out with CTAB to obtain a bundle of nanowires and a distinct nanorod morphology as discussed before. In particular, the sample NiCo–CH-180 prepared by adding 0.5 g CTAB shows a nanorod morphology (Fig. S5c, ESI†), which demonstrated the highest energy storage behavior (discussed later). The same sample was calcined at 500 °C for 2 h. The calcined NiCo–CH-180 sample shows similar morphology except for a rough surface as appeared in the FESEM image (Fig. S5d, ESI†). The morphology of the nanomaterials in turn influences the electrochemical properties due to the change in the specific surface area. The N_2 adsorption/desorption isotherms (Fig. S6, ESI†) are thus obtained through multi-point BET measurements at 77 K. The textural properties are presented in Table S2 (ESI†). It is found that NiCo–CH-180 has the highest specific surface area of 52.5 $m^2\ g^{-1}$, which is in good agreement with the FESEM analysis with an individual nanorod morphology rather than other morphologies, *i.e.*, bundle nanowires (Fig. 2(a)) at low temperature (120 °C) and microplates (Fig. 2(e)) at high temperature (200 °C). The microstructure and crystallographic properties of NiCo–CH-180 are studied using transmission electron microscopy. The TEM image (Fig. 2(f)) of NiCo–CH-180 correlates with the nanorod morphology. The SAED pattern (inset in the Fig. 2(f)) shows the crystalline nature of the synthesized sample. In particular, the rings with diffraction spots reveal the mono and polycrystalline nature of the nanorods.

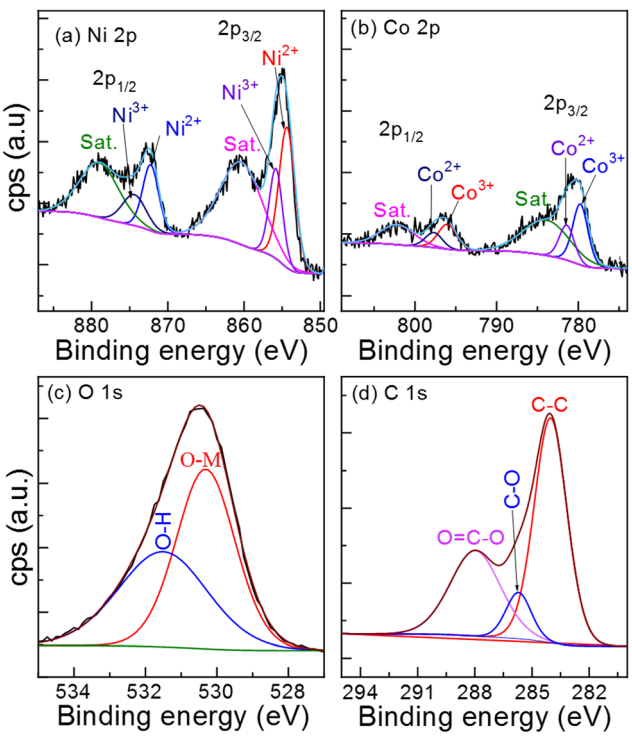

Fig. 3 High-resolution XPS spectra (a) Ni 2p, (b) Co 2p, (c) O 1s and (d) C 1s of NiCo–CH-180.

3.3 Elemental composition and oxidation states of Ni and Co

The elemental composition, *i.e.*, Ni : Co ratio of all the NiCo–CHs, synthesized at different experimental conditions, is

measured using EDS (Table S1, ESI†). The EDX spectra of the synthesized samples are presented in Fig. S7 (ESI†). At lower synthesis temperatures (120 and 140 °C), the Ni : Co atomic ratio is found to be close to 1 : 1 despite the higher (twice) initial Ni molar concentration. With an increase in the synthesis temperature, the atomic Ni% is found to increase and closely follows the initial molar concentration. The increase in atomic Ni% at higher synthesis temperature is correlated to the higher diffraction intensity for $Ni_2(CO_3)(OH)_2{\cdot}H_2O$ as shown in the XRD patterns (Fig. 1(a)). The higher Ni atomic % in the NiCo–CHs is found to play an important role in the electrochemical energy storage performance as discussed later.

The oxidation states of metals in NiCo–CH are measured using XPS measurement. The survey XPS spectrum (Fig. S8, ESI†) of NiCo–CH-180 confirms the presence of Ni, Co, O, and C elements on the surface of the material. Fig. 3(a) and (b) show the region XPS spectra of Ni 2p and Co 2p of NiCo–CH-180, respectively. The photoelectron peaks are deconvoluted using CasaXPS software. The position and area under the deconvoluted peaks are presented in Table S3 (ESI†). The Ni 2p region spectrum (Fig. 3(a)) shows peaks at 854.5 and 872.2 eV, which are assigned to the Ni^{2+} state. Another set of Ni 2p peaks at 856.1 and 874.4 eV confirms the Ni^{3+} states. Two broad peaks at 860.5 and 879.1 eV are the satellite peaks, which correspond to Ni $2p_{3/2}$ and Ni $2p_{1/2}$, respectively.[51,53] The region Co 2p XPS spectrum (Fig. 3(b)) reveals two spin–orbit doublets at the binding energy values of 781.4 eV (Co $2p_{3/2}$) and 797.7 eV (Co $2p_{1/2}$) for the Co^{2+} state along with two other spin-orbital binding energy peaks at 779.7 eV (Co $2p_{3/2}$) and 796 eV (Co $2p_{1/2}$) ascribed to the Co^{3+} state. Additionally, the two satellite peaks in the Co 2p spectrum are found at 783.9 and 802.2 eV that correspond to Co $2p_{3/2}$ and Co $2p_{1/2}$, respectively.[54] Fig. 3(c) shows the deconvoluted O 1s XPS spectrum, which reveals two fitted peaks at 531.4 and 530.3 eV, which correspond to hydroxyl groups (O–H) and metal oxygen bonds (O–Ni/Co), respectively.[55] The deconvoluted C 1s XPS spectrum (Fig. 3(d)) reveals the fitted peaks at 287.8, 285.7, and 284 eV, which are assigned to distinct functional groups of carboxylate carbon (O═C–O), carbon–oxygen single bonds (C–O), and aromatic linked carbon (C–C), respectively.[31] The XPS data reveal the multiple states of Ni and Co metals, *i.e.*, Ni^{2+}, Ni^{3+}, Co^{2+}, and Co^{3+} in the NiCo–CHs, which are advantageous for enhanced electrochemical performance. The detailed physicochemical characterizations including XRD, FTIR, and XPS confirm the successful formation of nickel–cobalt carbonate hydroxide hydrate.

3.4 Growth mechanism

In the solvothermal process, the metal salt precursors are first dissolved to their respective ions in water (H_2O), as shown in eqn (1) and (2). The ammonia (NH_3) and carbon dioxide (CO_2) are formed upon the hydrolysis of urea (eqn (3)).[56] The formed ions are gradually hydrolyzed to produce hydroxide ions (OH^-), ammonium ions (NH_4^+), and carbonate ions (CO_3^{2-}) (eqn (4) and (5)).[57] Finally, the hydroxide and carbonate ions react with nickel and cobalt ions to form nickel cobalt carbonate hydroxide (NiCo–CHs) (eqn (6) and (7)). The CTAB plays a crucial role in controlling the growth of the nanostructures.[58,59] Scheme 1 displays the formation of nickel–cobalt carbonate hydroxide with the required salt precursors.

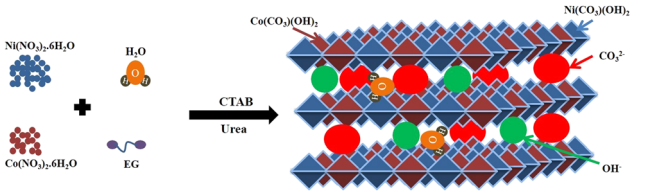

Scheme 1 Schematic representation of the synthesis of nickel–cobalt carbonate hydroxide.

$$Ni(NO_3)_2{\cdot}6H_2O \rightarrow Ni^{2+} + 2NO_3^- + 6H_2O \quad (1)$$

$$Co(NO_3)_2{\cdot}6H_2O \rightarrow Co^{2+} + 2NO_3^- + 6H_2O \quad (2)$$

$$H_2NCONH_2 + H_2O \rightarrow 2NH_3 + CO_2 \quad (3)$$

$$NH_3 + H_2O \rightarrow NH_4^+ + OH^- \quad (4)$$

$$CO_2 + 2OH^- \rightarrow CO_3^{2-} + H_2O \quad (5)$$

$$2Ni^{2+} + CO_3^{2-} + 2OH^- + H_2O \rightarrow Ni_2(CO_3)(OH)_2{\cdot}H_2O \quad (6)$$

$$2Co^{2+} + CO_3^{2-} + 2OH^- + 2H_2O \rightarrow 2Co(CO_3)_{0.5}(OH){\cdot}H_2O \quad (7)$$

3.5 Electrochemical analysis

3.5.1 Electrochemical measurement in a three-electrode system. The electrochemical measurements such as cyclic voltammetry (CV), galvanostatic charge discharge (GCD), and electrochemical impedance spectroscopy (EIS) of all the prepared materials are performed using a three-electrode system in a 2 M KOH aqueous electrolyte. The working electrode was prepared with NiCo–CH, AC, and PVDF with a weight ratio of 70 : 20 : 10. The reasons for choosing AC as a conducting agent to study the supercapacitor performance of the synthesized NiCo–CH electrode material were the cost-effectiveness, high good chemical stability, and negligible specific capacitance. In the studied potential range (−0.1 to 0.5 V SCE) in 2 M KOH electrolyte, the AC shows a negligible energy storage performance as shown in the CV profile (Fig. S9, ESI†). The CV curves of all the prepared NiCo–CH electrode materials are shown in Fig. 4(a) and Fig. S10a–S13a (ESI†). All the CV profiles show two broad redox peaks confirming the pseudocapacitive behavior of the NiCo–CH.[60] The CV profiles for the NiCo–CHs obtained at different synthesis temperatures are found to be slightly varied. In particular, NiCo–CH-180 shows a strong oxidation peak and more than one reduction peak. These observed variations in the CV can be attributed to the catalyst properties including morphology, crystallinity, and Ni : Co composition. The uniformity of the morphology and higher Ni : Co ratio of NiCo–CH-180 lead to a high structural stability resulting in a positive oxidation potential and manifestation of a single oxidation peak. Conversely, NiCo–CH in the oxidized form shows multiple reduction peaks corresponding to the cobalt and nickel

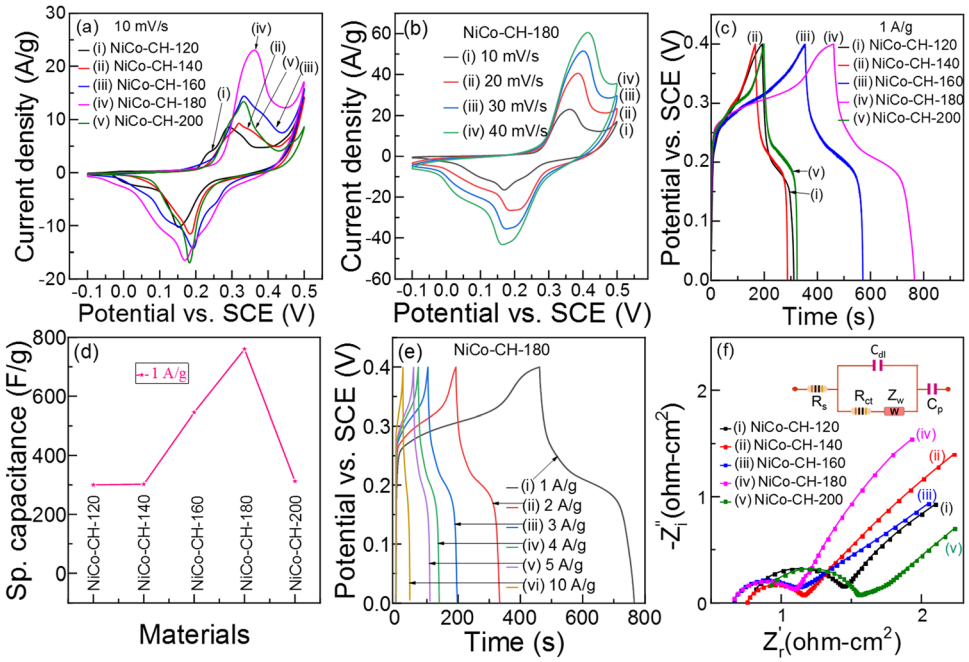

Fig. 4 (a) CV curves of NiCo–CHs synthesized at different temperatures. (b) CV curves of NiCo–CH-180 at different scan rates. (c) GCD plots at 1 A g^{-1} and (d) specific capacitance of the NiCo–CHs synthesized at different temperatures. (e) GCD plots of NiCo–CH-180 at different current densities. (f) Nyquist plots of NiCo–CHs synthesized at different temperatures.

phases. The electrochemical reactions are presented by eqn (8)–(12) that elucidate these intricate processes. First, NiCo–CH interacts with hydroxyl ions to create metal oxyhydroxides (eqn (8) and (9)) and then reversible transitions of $Ni^{2+} \leftrightarrow Ni^{3+}$ and $Co^{2+} \leftrightarrow Co^{3+} \leftrightarrow Co^{4+}$ as represented in eqn (10)–(12).[61,62]

$$Ni_2(CO_3)(OH)_2 + 4OH^- \leftrightarrow 2NiOOH + CO_3^{2-} + 2H_2O + 2e^- \quad (8)$$

$$2Co(CO_3)_{0.5}(OH) + 4OH^- \leftrightarrow 2CoOOH + CO_3^{2-} + H_2O + 2e^- \quad (9)$$

$$NiOOH + H_2O + e^- \leftrightarrow Ni(OH)_2 + OH^- \quad (10)$$

$$CoOOH + H_2O + e^- \leftrightarrow Co(OH)_2 + OH^- \quad (11)$$

$$CoOOH + OH^- \leftrightarrow CoO_2 + H_2O + e^- \quad (12)$$

Fig. 4(a) shows the CV profiles of NiCo–CH prepared at different solvothermal temperatures. The NiCo–CH-180 electrode shows the maximum area under the CV curve, indicating maximum charge storage capability among the prepared samples. This suggests that the uniform nanorod morphology with larger specific surface area (Table S2, ESI†) and higher Ni : Co ratio in the NiCo–CH-180 (Table S1, ESI†) play a significant role in enhancing the electrochemical energy storage performance. The repeatability of the electrochemical data is studied with three sets of experiments for NiCo–CH-180 and NiCo–CH-160 samples, which shows higher performance. The CV profiles of three NiCo–CH-180 and NiCo–CH-160 samples show similar curves (Fig. S14, ESI†) indicating high reproducibility. It is important to note that the shape of the CV curves of NiCo–CH-180 remains unchanged upon increasing the scan rate from 10 to 40 mV s^{-1} (Fig. 4(b)). Moreover, the anodic and cathodic peaks shifted toward more positive and negative potential, respectively, along with an increase in the current values. This tendency indicates a diffusion-controlled process. GCD measurements are performed for all the prepared electrode materials, as shown in Fig. 4(c) and Fig. S10b–S13b (ESI†). The non-linear shape of the charge and discharging curves matches the redox peaks in the CV curve, which confirms the faradaic charge storage mechanism. The specific capacitances (C_s) are calculated from the GCD curves using eqn (13) as listed in Table S4 at 1 A g^{-1} current density in a potential window of 0 to 0.4 V. Fig. 4(d) shows the C_s values of the electrode materials synthesized by varying the reaction temperature. Among the synthesized samples, NiCo–CH-180 showed the highest capacitance value of 762 F g^{-1}. The C_s and Coulombic efficiency (η) values of all the synthesized samples are listed in Table S4 (ESI†). The highest C_s value of NiCo–CH-180 is attributed to its well separated nanorods with the highest specific surface area. Fig. 4e shows the GCD plots of the NiCo–CH-180 electrode at different current densities. The C_s values are estimated to be 762, 720, 698, 630, 663, and 550 F g^{-1} at 1, 2, 3, 4, 5, and 10 A g^{-1} applied current density, respectively. A 27.8% reduction of C_s value of NiCo–CH-180 is found by increasing the current density from 1 to 10 A g^{-1}, which is due to insufficient time for electrolyte ions to diffuse into the pores and interact with the active center of the surface. On the other hand, a greater number of electrolytic ions diffuse into the electrode material pores and interact with the active surface at lower applied current density.[62] To study the stability of the best performing electrode material (*i.e.*, NiCo–CH-180), GCD

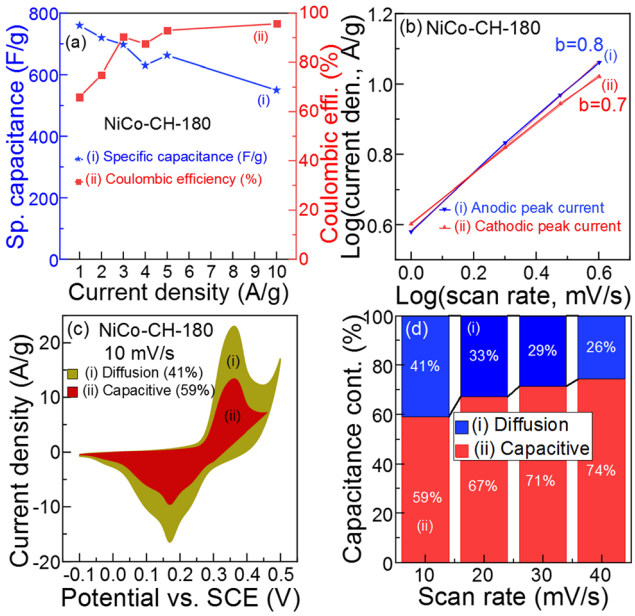

Fig. 5 (a) Specific capacitance and coulombic efficiency of NiCo–CH-180 at different current densities, (b) linear logarithmic plots of current density *versus* scan rate, (c) the CV curve with diffusion and capacitive capacitance contribution at 10 mV s^{-1}, and (d) diffusion and capacitive capacitance contribution at different scan rates of NiCo–CH-180.

measurements were performed for 5000 cycles in 2 M KOH electrolyte at a higher applied current density (20 A g^{-1}) (Fig. S15a, ESI†). The post electrochemical measurement confirms the original nanorod morphology of NiCo–CH-180 as confirmed in the FESEM image (Fig. S15b, ESI†) suggesting stability of the electrode material.

The coulombic efficiency (η) is further estimated by taking the ratio of discharging time and charging time (eqn (14)) from the GCD plots.

$$C_s = \frac{I \times t_d}{m \times \Delta V} \quad (13)$$

$$\eta = \frac{t_d}{t_c} \quad (14)$$

where, C_s, I, t_d, t_c, m, ΔV, and η are the specific capacitance (F g^{-1}), current (A), discharge time (s), charge time (s), active material's mass (g), potential window, and coulombic efficiency (%), respectively. The specific capacitance and coulombic efficiency of the prepared electrode materials are shown in Fig. 5(a) and Fig. S10c–S13c (ESI†). The highest 762 F g^{-1} specific capacitance at 1 A g^{-1} current density is obtained for NiCo–CH-180 (12 h) nanorods. Although the C_s value is found to be maximum for NiCo–CH-180 (12 h) due to the uniform nanorod morphology, the η is the highest for NiCo–CH-180 (48 h), which shows nanorods and microplate morphology. The higher η values are believed to be due to the intrinsic properties of materials synthesized for a longer synthesis duration. To understand the electrochemical performance of the different electrode materials, EIS measurements were performed in an aqueous electrolyte of 2 M KOH through Nyquist plots as shown in Fig. 4f and Fig. S10d–S13d (ESI†). The inset in Fig. 4(f) shows an equivalent circuit diagram that is used to fit the Nyquist plots. A semicircle and a straight line in the Nyquist plots are found in the high and low frequency range, respectively. The solution resistance (R_s) is observed on the real axis in the high frequency region. The charge-transfer resistance (R_{ct}) is determined from the diameter of the semicircle at high to intermediate frequencies. The linear part of the Nyquist plot in the low frequency region is due to the diffusion of electrolytic ions into the active electrode material and represents the Warburg impedance.[63] From the Nyquist plots, solution resistance (R_s), charge-transfer resistance (R_{ct}), Warburg impedance (Z_w), electric double capacitance (C_{dl}), and pseudocapacitance (C_p) are measured using equivalent circuit fitting and all the major parameters are listed in Table S4. The smallest charge-transfer resistance of 0.36 Ω cm^2 is obtained with NiCo–CH-180 indicating better charge transportation and ion diffusion mechanism than for other electrode materials. The Nyquist plot under consideration also shows a linear part described by the Warburg impedance, which demonstrates penetration of the electrolyte ions into the active electrode material.[64] Furthermore, the best performing electrode material, *i.e.*, NiCo–CH-180, is calcined at 500 °C for 2 h to study its performance for energy storage. The specific capacitance value of the calcined sample is decreased by 45% (*i.e.*, from 762 to 417 F g^{-1}), which correlates to an increased R_{ct} and R_s from 0.36 to 1.8 Ω cm^2 and from 0.66 to 9.4 Ω cm^2 respectively, demonstrating a decrease in electronic conductivity.

To understand the charge storage mechanism and reaction kinetics, CV analysis of the electrode material (NiCo–CH-180) was performed at low scan rates of 1 to 4 mV s^{-1} (Fig. S16, ESI†). In particular, this analysis provides the percentage of ions that undergo the diffusion-controlled process and ion intercalation on the electrode. The overall effect of diffusive and capacitive behavior of the synthesized electrode material is estimated by using the Power law as represented by eqn (15).[65]

$$i = a\nu^b \quad (15)$$

$$\log(i) = \log(a) + b\log(\nu) \quad (16)$$

where i is the anodic or cathodic peak, ν is the scan rate, a is a constant and b is a constant that is used to define the charge storage mechanism. The b value is calculated from the slope of the linear portion of log (i) *vs.* log (ν) using eqn (15), where the b value of 1 represents the EDLC type (surface controlled contribution), the b value of 0.5 represents the pseudocapacitor type (pure diffusion controlled-contribution), a b value between 0.5 to 1 represents the pseudocapacitive type (*i.e.*, both surface and diffusion controlled contribution), and a b value <0.5 represents the battery-type (bulk diffusion controlled faradaic processes).[66] In the present work, the b values of 0.8 and 0.7 were calculated for the prepared electrode materials using the anodic and cathodic peak current, respectively, at low scan rate by linear fitting of eqn (16), as shown in Fig. 5(b). The obtained b value reveals a combined effect of extrinsic charge storage intercalation, *i.e.*, capacitive and diffusion-controlled faradaic contribution, which demonstrates the pseudocapacitive nature

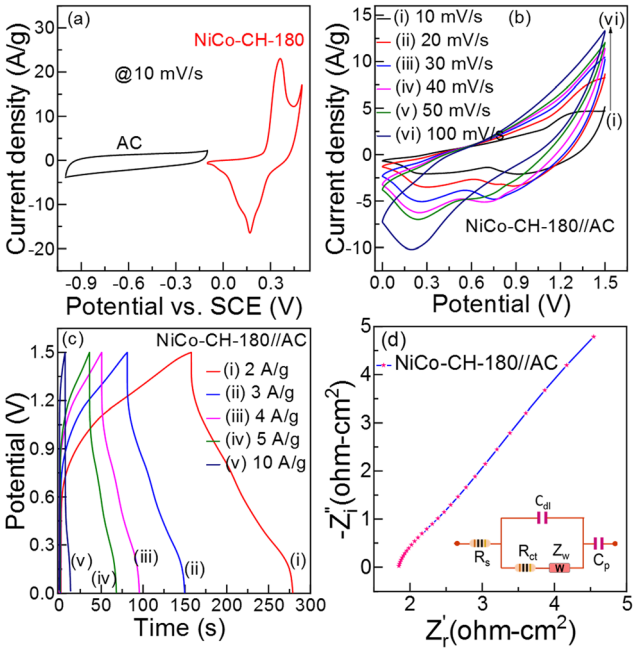

Fig. 6 (a) CV curve of the negative (AC) and positive (NiCo–CH-180) electrode at 10 mV s^{-1} in a three-electrode set up. (b) CV curves for the ASC at various scan rates (10–100 mV s), (c) GCD curves at different current densities (2–10 A g^{-1}), and (d) Nyquist plot of the NiCo–CH-180//AC ASC (two-electrode device).

of the NiCo–CH-180.[67] The percentage of capacitive and diffusion-controlled contribution is calculated using eqn (17).[68]

$$i\,(V) = k_1\nu + k_2\nu^{1/2} \quad (17)$$

where i and ν are the current at the defined voltage and scan rate, and k_1 and k_2 are constants. The capacitive and diffusion-controlled behavior terms are $k_1\nu$ and $k_2\nu^{1/2}$, respectively. Fig. 5(c) shows the CV of NiCo–CH-180 at 10 mV s^{-1}, which suggests more capacitive controlled contribution (*i.e.*, 59%) than diffusion-controlled contribution (*i.e.*, 41%). This reveals that the electrode material has larger surface area and more electrochemical active sites for the surface ion intercalation. The capacitance contribution at different scan rates is presented in Fig. 5(d). With an increase in the scan rate, the diffusion-controlled contribution decreases because there is no sufficient time to diffuse the ions into the pore or in the interstitial sites of the prepared electrode materials at higher scan rate. According to the characterization results, the NiCo–CH-180 shows an optimal structure, shape, and size with a high pore volume and surface area that provides the maximum active surface for the faradaic reaction, intercalation, and diffusion resulting in enhanced supercapacitor performance.

3.5.2 Electrochemical performance of the asymmetric supercapacitor (ASC). From the three-electrode electrochemical measurements, NiCo–CH-180 is found to show the best electrochemical storage performance among the synthesized samples. Thus NiCo–CH-180 is used as a positive electrode material and activated carbon (AC) as a negative electrode material in fabricating a two-electrode asymmetric device. Fig. 6(a) shows the CV curves of NiCo–CH-180 and AC in the potential windows of −0.1 to 0.5 V and −1.0 to −0.1 V at 10 mV s^{-1}, respectively. Using CV, the charge balance is maintained by adjusting the weight of the NiCo–CH-180 (+ve) and AC (−ve) electrodes using eqn (18) to obtain the best ASC performance.[69]

$$\frac{W_+}{W_-} = \frac{C_- \times \Delta V_-}{C_+ \times \Delta V_+} \quad (18)$$

where W_+/W_-, C_+/C_- and $\Delta V_+/\Delta V_-$ are the weight of the positive/negative electrode materials, capacitances, and potential windows, respectively. For the two-electrode solid-state ASC device, PVA + KOH gel is used as an electrolyte and Whatman filter paper as a separator. The CV curves (Fig. 6(b)) of the NiCo–CH-180//AC ASC device at various scan rates exhibit a non-rectangular shape in the potential range of 0 to 1.5 V, which indicates the faradaic nature of charge storage. The absence of distinct redox peaks in the CV curve in the all-solid-state ASC device suggests slow kinetics of the electrochemical reactions occurring at the electrode/electrolyte interface due to the solid-state electrolyte. This sluggish behavior is linked to high charge-transfer resistance, slow ion diffusion, or limited accessibility of active sites unlike the three-electrode system with liquid electrolyte. The GCD measurements were performed on the fabricated ASC at different applied current densities. The GCD plots (Fig. 6(c)) corroborate the pseudocapacitance behavior of the NiCo–CH-180. The electrochemical kinetics of the ASC NiCo–CH-180//AC device are analyzed by performing EIS measurement in the frequency range of 0.1 Hz to 1 MHz. The Nyquist plot with a fitted circuit diagram is shown in Fig. 6(d). A low R_{ct} (0.38 Ω cm^2) suggests the charge transport activity at the electrode and electrolyte interface. Moreover, the

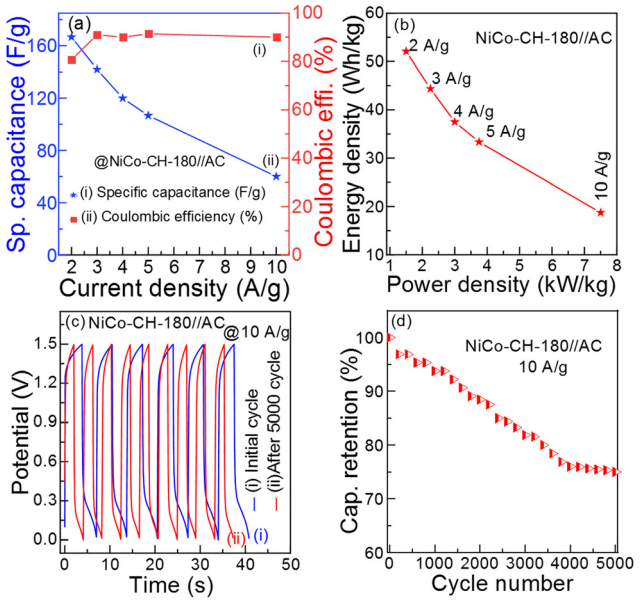

Fig. 7 (a) Specific capacitance and coulombic efficiency of NiCo–CH-180//AC ASC at different current densities (2–10 A g^{-1}), (b) Ragone plot (ED *vs.* PD), (c) initial and after 5000 charge–discharge curves, and (d) capacitance retention performance up to 5000 charge–discharge cycles at 10 A g^{-1} current density of the NiCo–CH-180//AC ASC.

Table 1 Comparison of the ASC performance of the NiCo–CH-180/AC device with related electrode materials

Electrode materials for the ASC device	Specific capacitance (F g^{-1})	Current density (A g^{-1})	Energy density (W h kg^{-1})	Power density (W kg^{-1})	Ref.
$Co_2(CO_3)(OH)_2$ NDs/$NiCo(CO_3)(OH)_2$//graphene	128	2	35.5	2555	17
$NiCu(OH)_2CO_3$//AC	476	1	48.55	541	22
$Cu_{1.79}Co_{0.21}$CH/NF//graphene/NF	60	1	21.5	200	31
Co1Ni1//AC	106	1	42.5	850	42
NF@Co–CH@NiCoMn–CH//AC	169	1	20.3	748	45
MnNiCo–CH/CF//CNT	96	1	30.04	750	55
$(Ni_{0.89}Cu_{0.11})_2(OH)_2CO_3$//AC@Ni foam	96	1	38.56	850	60
$Ni_1Co_1Zn_{0.25}$–CH//AC	94.7	1	33.7	400	40
NiCo–CH-180//AC	125	2	52	1500	This work

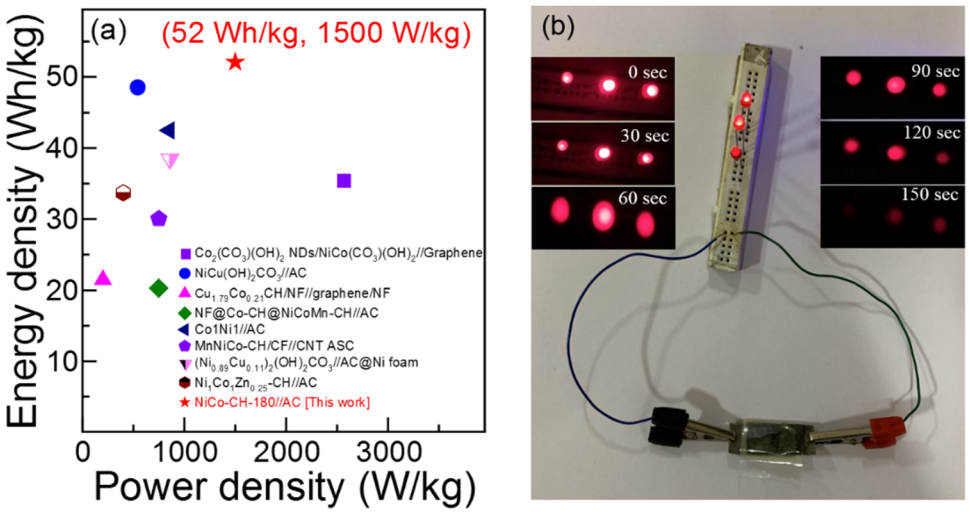

Fig. 8 (a) Ragone plot of NiCo–CH-180//AC compared with the literature on devices with similar electrode materials and (b) photograph of a device to light three red LEDs.

absence of a semicircle feature in the Nyquist plot of the EIS indicates limited charge transfer reactions due to the solid electrolyte/electrode interface.

The C_s, coulombic efficiency, energy density, and power density of the NiCo–CH-180//AC ASC device are calculated by using eqn (13), (14), (19) and (20) from the GCD curves.[16]

$$\mathrm{ED} = \frac{C_s \times \Delta V^2}{7200} \tag{19}$$

$$\mathrm{PD} = \frac{3600 \times \mathrm{ED}}{t_d} \tag{20}$$

where ED, PD, C_s, ΔV, and t_d represent the energy density (W h kg^{-1}), power density (W kg^{-1}), specific capacitance (F g^{-1}), potential window (V), and discharging time (s), respectively. Fig. 7(a) (C_s and coulombic efficiency) and Fig. 7(b) (ED and PD) show the performance of the ASC NiCo–CH-180//AC device. The detailed electrochemical performances of the fabricated device are presented in Table S5 (ESI†). The energy storage performance of the fabricated ASC of NiCo–CH-180//AC device is compared with the literature taking similar types of electrode materials as presented in Table 1 and Fig. 8(a). The ED and PD values of the fabricated ASC NiCo–CH-180//AC are found to be higher and/or comparable with the literature. The stability of the ASC NiCo–CH-180//AC device is tested by performing 5000 charge–discharge cycles at 10 A g^{-1} current density. Fig. 7(c) shows the initial and 5000 cycle GCD curve. The capacitance retention as a function of GCD cycle number is shown in Fig. 7(d), which exhibits 76.2% capacitance retention after 5000 charge–discharge cycles at the current density of 10 A g^{-1}. In the initial 4000 cycles, the capacitance retention is decreased linearly and becomes saturated. The decreased performance is suggested to be due to structural changes and/or formation of undesired products with charge and discharge cycles. Additionally, the electrolyte decomposition, solid–electrolyte interface growth, and other electrochemical processes can contribute to the observed degradation. Moreover, the capacitance of >75% at a high current density (10 A g^{-1}) suggests good cycling stability of the electrode material, *i.e.*, NiCo–CH-180. To demonstrate the practical application of the fabricated ASC NiCo–CH-180//AC device, three 1.5 V red light-emitting diodes (LEDs) were lit for 150 s (Fig. 8) after charging for 3 min.

4. Conclusions

In this work, we demonstrate the successful synthesis of nickel–cobalt carbonate hydroxide by the solvothermal method by

varying different reaction parameters. The reaction parameters play an important role in controlling the morphology and Ni : Co ratio of the products. In particular, an optimized precursor concentration (2 : 1 Ni : Co precursor ratio), reaction temperature (180 °C), growth duration (12 h), and mixed solvent (15 mL EG +20 mL H_2O) medium with CTAB as a surfactant lead to a uniform nanorod morphology of the sample (NiCo–CH-180) with improved electrochemical energy storage performance. The NiCo–CH-180 exhibits a higher specific capacitance of 762 F g^{-1} at 1 A g^{-1} current density and also shows excellent rate performance compared to other morphologies of NiCo–CH due to higher effective surface area and higher Ni : Co ratio of the former. From the detailed characterization of the synthesized materials, the NiCo–CH-180 is found to show an optimal structural combination and shape with a higher surface area, providing the maximum specific capacitance. A two-electrode ASC (NiCo–CH-180//AC) is fabricated with NiCo–CH-180 and AC as a positive and negative electrode material, respectively, which delivers the maximum energy density of 52 W h kg^{-1} at a power density of 760 W kg^{-1} and good cycling stability with the capacitance retention more than 75% after 5000 charge–discharge cycles at 10 A g^{-1}. This suggests the importance of the optimization of the morphology of the NiCo–CH for the improved supercapacitor performance.

Author contributions

Sudhir Kumar – conceptualization, data curation, formal analysis, investigation, methodology, validation, original draft; Biraj Kanta Satpathy – formal analysis, validation; Debabrata Pradhan – funding acquisition, project administration, resources, supervision, writing – review and editing.

Conflicts of interest

The authors declare no competing financial interest.

Acknowledgements

The current work was supported by DST, Govt. of India through the grant DST/TMD/MES/2K18/26(G). SK acknowledges the Indian Institute of Technology Kharagpur, India for a research fellowship. The authors acknowledge the Central Research Facility, IIT Kharagpur, and the DST-FIST funded FESEM facility at Materials Science Centre, IIT Kharagpur.

References

1 S. A. Matlin, G. Mehta, S. E. Cornell, A. Krief and H. Hopf, Chemistry and Pathways to Net Zero for Sustainability, *RSC Sustain.*, 2023, **1**, 1704–1721, DOI: 10.1039/D3SU00125C.

2 A. I. Osman, L. Chen, M. Yang, G. Msigwa, M. Farghali, S. Fawzy, D. W. Rooney and P. S. Yap, Cost, Environmental Impact, and Resilience of Renewable Energy under a Changing Climate: A Review, *Environ. Chem. Lett.*, 2022, **21**(2), 741–764, DOI: 10.1007/s10311-022-01532-8.

3 A. N. K. Lup, V. Soni, B. Keenan, J. Son, M. R. Taghartapeh, M. M. Morato, Y. Poya and R. M. Montañés, Sustainable Energy Technologies for the Global South: Challenges and Solutions Toward Achieving SDG 7, *Environ. Sci.: Adv.*, 2023, **2**, 570–585, DOI: 10.1039/D2VA00247G.

4 A. Rahman, O. Farrok and M. M. Haque, Environmental Impact of Renewable Energy Source Based Electrical Power Plants: Solar, Wind, Hydroelectric, Biomass, Geothermal, Tidal, Ocean, and Osmotic, *Renewable Sustainable Energy Rev.*, 2022, **161**, 112279, DOI: 10.1016/j.rser.2022.112279.

5 A. Z. A. Shaqsi, K. Sopian and A. Al-Hinai, Review of Energy Storage Services, Applications, Limitations, and Benefits, *Energy Rep.*, 2020, **6**, 288–306, DOI: 10.1016/j.egyr.2020.07.028.

6 J. Liu, Z. Huang, M. Fan, J. Yang, J. Xiao and Y. Wang, Future Energy Infrastructure, Energy Platform and Energy Storage, *Nano Energy*, 2022, **104**, 107915, DOI: 10.1016/j.nanoen.2022.107915.

7 J. Sun, B. Luo and H. Li, A Review on the Conventional Capacitors, Supercapacitors, and Emerging Hybrid Ion Capacitors: Past, Present, and Future, *Adv. Energy Sustainability Res.*, 2022, **3**, 2100191, DOI: 10.3390/chemengineering6010005.

8 D. P. Chatterjee and A. K. Nandi, A Review on the Recent Advances in Hybrid Supercapacitors, *J. Mater. Chem. A*, 2021, **9**, 15880–15918, DOI: 10.1016/j.ensm.2018.12.018.

9 A. A. Kamel, H. Rezk and M. A. Abdelkareem, Enhancing the Operation of Fuel Cell-Photovoltaic-Battery-Supercapacitor Renewable System through a Hybrid Energy Management Strategy, *Int. J. Hydrogen Energy*, 2021, **46**(8), 6061–6075, DOI: 10.1016/j.ijhydene.2020.06.052.

10 N. M. Santhosh, K. K. Upadhyay, P. Stražar, G. Filipič, J. Zavašnik, A. M. de Ferro, R. P. Silva, E. Tatarova, M. de Fátima Montemor and U. Cvelbar, Advanced Carbon–Nickel Sulfide Hybrid Nanostructures: Extending the Limits of Battery-Type Electrodes for Redox-Based Supercapacitor Applications, *ACS Appl. Mater. Interfaces*, 2021, **13**(17), 20559–20572, DOI: 10.1021/acsami.1c03053.

11 S. Fleischmann, J. B. Mitchell, R. Wang, C. Zhan, D. E. Jiang, V. Presser and V. Augustyn, Pseudocapacitance: From Fundamental Understanding to High Power Energy Storage Materials, *Chem. Rev.*, 2020, **120**(14), 6738–6782, DOI: 10.1021/acs.chemrev.0c00170.

12 A. G. Olabi, Q. Abbas, M. A. Abdelkareem, A. H. Alami, M. Mirzaeian and E. T. Sayed, Carbon-Based Materials for Supercapacitors: Recent Progress, Challenges and Barriers, *Batteries*, 2023, **9**(1), 19, DOI: 10.3390/batteries9010019.

13 J. E. Nady, A. Shokry, M. Khalil, S. Ebrahim, A. M. Elshaer and M. Anas, One-step Electrodeposition of a Polypyrrole/NiO Nanocomposite as a Supercapacitor Electrode, *Sci. Rep.*, 2022, **12**, 3611, DOI: 10.1038/s41598-022-07483-y.

14 S. Jangu, S. Kumar, K. N. Deepika, C. Jacob and D. Pradhan, Effect of Microwave Power and Cu Doping on MnO_2 Nanostructure on Its Supercapacitor Performance, *ACS Appl. Electron. Mater.*, 2023, **5**(6), 3078–3092, DOI: 10.1021/acsaelm.3c00152.

15 B. K. Satpathy, A. K. Nayak, C. R. Raj and D. Pradhan, Morphology-Dependent Charge Storage Performance of Co_3O_4 Nanostructures in an All-Solid-State Flexible Supercapacitor, *New J. Chem.*, 2019, **43**(38), 15177–15186, DOI: **10.1039/c9nj03070k**.

16 B. K. Satpathy, S. Patnaik and D. Pradhan, Room-Temperature Growth of $Co(OH)_2$ Nanosheets on Nanobelt-like $Cu(OH)_2$ Arrays for a Binder-Free High-Performance All-Solid-State Supercapacitor, *ACS Appl. Energy Mater.*, 2022, **5**(1), 77–87, DOI: **10.1021/acsaem.1c02398**.

17 D. Lee, Q. X. Xia, J. M. Yun and K. H. Kim, High-Performance Cobalt Carbonate Hydroxide Nano-Dot/$NiCo(CO_3)(OH)_2$Electrode for Asymmetric Supercapacitors, *Appl. Surf. Sci.*, 2018, **433**, 16–26, DOI: **10.1016/j.apsusc.2017.10.066**.

18 J. Cherusseri, N. Choudhary, K. S. Kumar, Y. Jung and J. Thomas, Recent Trends in Transition Metal Dichalcogenide Based Supercapacitor Electrodes, *Nanoscale Horiz.*, 2019, **4**(4), 840–858, DOI: **10.1039/c9nh00152b**.

19 B. C. Patra, S. Khilari, L. Satyanarayana, D. Pradhan and A. Bhaumik, A New Benzimidazole Based Covalent Organic Polymer Having High Energy Storage Capacity, *Chem. Commun.*, 2016, **52**(48), 7592–7595, DOI: **10.1039/c6cc02011a**.

20 Y. Han and L. Dai, Conducting Polymers for Flexible Supercapacitors, *Macromol. Chem. Phys.*, 2019, **220**, 1800355, DOI: **10.1002/macp.201800355**.

21 X. Li and J. Wang, One-Dimensional and Two-Dimensional Synergized Nanostructures for High-Performing Energy Storage and Conversion, *InfoMat*, 2020, **2**(1), 3–32, DOI: **10.1002/inf2.12040**.

22 X. Zheng, Y. Ye, Q. Yang, B. Geng and X. Zhang, Ultrafine Nickel-Copper Carbonate Hydroxide Hierarchical Nanowire Networks for High-Performance Supercapacitor Electrodes, *Chem. Eng. J.*, 2016, **290**, 353–360, DOI: **10.1016/j.cej.2016.01.076**.

23 A. Karmakar, H. S. Chavan, S. M. Jeong and J. S. Cho, Mixed Transition Metal Carbonate Hydroxide-Based Nanostructured Electrocatalysts for Alkaline Oxygen Evolution: Status and Perspectives, *Adv. Energy Sustainability Res.*, 2022, **3**(9), 2200071, DOI: **10.1002/aesr.202200071**.

24 S. H. Baek, Y. M. Jeong, D. Y. Kim and I. K. Park, Phase Transformation of NiCo Hydroxides Derived from Carbonate Anion and Its Effect on Electrochemical Pseudocapacitor Performance, *Chem. Eng. J.*, 2020, **393**, 124713, DOI: **10.1016/j.cej.2020.124713**.

25 J. W. Boclair and P. S. Braterman, Layered Double Hydroxide Stability. 1. Relative Stabilities of Layered Double Hydroxides and Their Simple Counterparts, *Chem. Mater.*, 1999, **11**(2), 298–302, DOI: **10.1021/cm980523u**.

26 W. Hu, L. Chen, B. Geng, Y. Song, Z. Wu, Q. Zheng, G. Shan and M. Du, Effect of Intercalated Anion in Nickel–Cobalt-Layered Double Hydroxide on Its Supercapacitive Properties, *Chem. Eng. J.*, 2023, **468**, 143694, DOI: **10.1016/j.cej.2023.143694**.

27 T. Kokulnathan, T. J. Wang, E. A. Kumar and F. Ahmed, Construction of Nickel Cobalt-Layered Double Hydroxide/Functionalized–Halloysite Nanotubes Composite for Electrochemical Detection of Organophosphate Insecticide, *Chem. Eng. J.*, 2022, **433**, 133639, DOI: **10.1016/j.cej.2021.133639**.

28 Y. Wang, Y. Liu, Z. Chen, M. Zhang, B. Liu, Z. Xu and K. Yan, *In Situ* Growth of Hydrophilic Nickel-Cobalt Layered Double Hydroxides Nanosheets on Biomass Waste-Derived Porous Carbon for High-Performance Hybrid Supercapacitors, *Green, Chem. Eng.*, 2022, **3**(1), 55–63, DOI: **10.1016/j.gce.2021.09.001**.

29 M. Shi, M. Zhao, L. Jiao, Z. Su, M. Li and X. Song, Novel Mo-Doped Nickel Sulfide Thin Sheets Decorated with Ni–Co Layered Double Hydroxide Sheets as an Advanced Electrode for Aqueous Asymmetric Super-Capacitor Battery, *J. Power Sources*, 2021, **509**, 230333, DOI: **10.1016/j.jpowsour.2021.230333**.

30 S. Gayathri, P. Arunkumar, J. Kim and J. H. Han, Bimetallic Layered Hydroxide Nitrate@Graphene Oxide as an Electrocatalyst for Efficient Non-Enzymatic Glucose Sensors: Tuning Sensitivity by Hydroxide-Regulated $M_2(OH)_4$-$n(A^{n-})$ Phases Derived from Solvent Engineering, *ACS Sustainable Chem. Eng.*, 2022, **10**(4), 1689–1701, DOI: **10.1021/acssuschemeng.1c07644**.

31 S. Liu, K. S. Hui, K. N. Hui, V. V. Jadhav, Q. X. Xia, J. M. Yun, Y. R. Cho, R. S. Mane and K. H. Kim, Facile Synthesis of Microsphere Copper Cobalt Carbonate Hydroxides Electrode for Asymmetric Supercapacitor, *Electrochim. Acta*, 2016, **188**, 898–908, DOI: **10.1016/j.electacta.2015.12.018**.

32 X. Wang, X. Li, X. Du, X. Ma, X. Hao, C. Xue, H. Zhu and S. Li, Controllable Synthesis of NiCo LDH Nanosheets for Fabrication of High-Performance Supercapacitor Electrodes, *Electroanalysis*, 2017, **29**(5), 1286–1293, DOI: **10.1002/elan.201600602**.

33 B. P. Bastakoti, Y. Kamachi, H. S. Huang, L. C. Chen, K. C. W. Wu and Y. Yamauchi, Hydrothermal Synthesis of Binary Ni-Co Hydroxides and Carbonate Hydroxides as Pseudosupercapacitors, *Eur. J. Inorg. Chem.*, 2013, 39–43, DOI: **10.1002/ejic.201200939**.

34 Y. Li, P. Li, Z. Xin, Z. Sun and M. Cao, and Luhai Li, Hydrothermal Synthesis of Hierarchical Nickel- or Cobalt Based Carbonate Hydroxides for Supercapacitor Electrodes, *Int. J. Electrochem. Sci.*, 2017, **12**, 4016–4024, DOI: **10.20964/2017.05.50**.

35 D. Le, Q. X. Xia, J. M. Yun and K. H. Kim, High-performance Cobalt Carbonate Hydroxide Nano-dot/$NiCo(CO_3)(OH)_2$ Electrode for Asymmetric Supercapacitors, *Appl. Surf. Sci.*, 2018, **433**, 16–26, DOI: **10.1016/j.apsusc.2017.10.066**.

36 G. Zhang, P. Qin, R. Nasser, S. Li, P. Chen and J. Song, Synthesis of $Co(CO_3)_{0.5}(OH)$/$Ni_2(CO_3)(OH)_2$ Nanobelts and Their Application in Flexible All-solid-state Asymmetric Supercapacitor, *Chem. Eng. J.*, 2020, **387**, 124029, DOI: **10.1016/j.cej.2020.124029**.

37 N. Poompiew, P. Pattananuwat and P. Potiyaraj, Controllable Morphology of Sea-Urchin-like Nickel–Cobalt Carbonate Hydroxide as a Supercapacitor Electrode with Battery-like Behavior, *ACS Omega*, 2021, **6**(39), 25138–25150, DOI: **10.1021/acsomega.1c02139**.

38 J. Wang, D. Zhang, W. She, S. Gao, K. Wang, Y. Wang, Z. Han, X. Chen and L. Li, Flower-like NiCo-carbonate Hydroxides for High performance Solid-state Hybrid

Supercapacitor, *Electroanalysis*, 2022, **34**, 1121–1130, DOI: 10.1002/elan.202100542.

39 Z. Shi, Y. Yuan, Q. Xiao, Z. Li and J. Zhu, Carbonate Doped NiCo-LDH Modified with PANI for High Performance Asymmetric Supercapacitors, *CrystEngComm*, 2022, **24**, 3546–3555, DOI: 10.1039/D2CE00241H.

40 R. Liu, X. Gao, Y. Xie, Q. Liu, K. Zhang, Y. Sun, H. Bai, F. Yao and H. Yu, Self-templated Flower-like NiCoZn-carbonate Hydroxide Hollow Nanospheres for Asymmetric Supercapacitors with High Performance, *Nanoscale*, 2023, **15**, 16795–16802, DOI: 10.1039/D3NR03839D.

41 A. George and M. Kundu, Exchanging Anion in CuCo Carbonate Double Hydroxide for faradaic Supercapacitors: A Case Study, *ACS Omega*, 2023, **8**, 17028–17042, DOI: 10.1021/acsomega.3c01211.

42 X.-L. Wang, G.-F. Zhang, R. Nasser, T.-T. Jiang, Q.-W. Cao, M. Gong, X.-Y. Li and J.-M. Song, Controllable Synthesis of Co/Ni Basic Carbonate Composite *via* Regulating Co/Ni Ratio with Super Rate Performance for Asymmetric Solid-state Supercapacitor, *J. Alloys Compd.*, 2022, **906**, 164270, DOI: 10.1016/j.jallcom.2022.164270.

43 M. Bhatt, A. K. Sinha, P. Bhojane, M. N. Singh and M. Gupta, Structural and Electronic Properties of Nickel–cobalt Carbonate Hydroxide Hydrate Nanostructures for High Performance Supercapacitor Applications, *J. Mater. Sci.: Mater. Electron.*, 2023, **34**, 1933, DOI: 10.1007/s10854-023-11391-w.

44 P. Bhojane, L. Sinha, U. K. Goutam and P. M. Shirage, A 3D Mesoporous Flowers of Nickel Carbonate Hydroxide Hydrate for High-Performance Electrochemical Energy Storage Application, *Electrochim. Acta*, 2019, **296**, 112–119, DOI: 10.1016/j.electacta.2018.11.025.

45 Y. Zhong, X. Cao, Y. Liu, L. Cui and J. Liu, Nickel Cobalt Manganese Ternary Carbonate Hydroxide Nanoflakes Branched on Cobalt Carbonate Hydroxide Nanowire Arrays as Novel Electrode Material for Supercapacitors with Outstanding Performance, *J. Colloid Interface Sci.*, 2021, **581**, 11–20, DOI: 10.1016/j.jcis.2020.07.124.

46 Y. Hu, A. Chaka and D. A. Dixon, Thermodynamics of the Metal Carbonates and Bicarbonates of Mn, Co, Ni, Cu, and Zn Relevant to Mineral Energetics, *J. Phys. Chem. A*, 2022, **126**(43), 7874–7887, DOI: 10.1021/acs.jpca.2c05341.

47 H. Yang, L. Yuan, M. Yuan and P. Ning, Insight into the Mechanism of Cobalt-Nickel Separation Using DFT Calculations on Ethylenediamine-Modified Silica Gel, *Materials*, 2023, **16**, 3445, DOI: 10.3390/ma16093445.

48 R. L. Frost, M. J. Dickfos and B. J. Reddy, Raman Spectroscopy of Hydroxy Nickel Carbonate Minerals Nullaginite and Zaratite, *J. Raman Spectrosc.*, 2008, **39**(9), 1250–1256, DOI: 10.1002/jrs.1978.

49 J. Yang, H. Cheng and R. L. Frost, Synthesis and Characterisation of Cobalt Hydroxy Carbonate $Co_2CO_3(OH)_2$ Nanomaterials, *Spectrochim. Acta, Part A*, 2011, **78**(1), 420–428, DOI: 10.1016/j.saa.2010.11.004.

50 M. R. Rahman, B. Riscob, R. Bhatt, I. Bhaumik, S. Ganesamoorthy, N. Vijayan, G. Bhagavannarayana, A. K. Karnal and L. Nair, Investigations on Crystalline Perfection, Raman Spectra and Optical Characteristics of Transition Metal (Ru) Co-doped Mg: $LiNbO_3$ Single Crystals, *ACS Omega*, 2021, **6**(16), 10807–10815, DOI: 10.1021/acsomega.1c00452.

51 S. Xiu, H. T. Jung, B. Quan and C. J. An, Intimately Interconnected Nickel Carbonate Hydroxide Nanosheet-Wire Structure for High-Performance Asymmetric Supercapacitors, *Int. J. Energy Res.*, 2022, **46**(14), 19667–19677, DOI: 10.1002/er.8530.

52 O. Guellati, A. Harat, D. Momodu, J. Dangbegnon, T. Romero, D. Begin, C. Pham-Huu, N. Manyala and M. Guerioune, Electrochemical Measurements of 1D/2D/3DNi-Co Bi-Phase Mesoporous Nanohybrids Synthesized Using Free-Template Hydrothermal Method, *Electrochim. Acta*, 2018, **275**, 155–171, DOI: 10.1016/j.electacta.2018.04.112.

53 D. Ghosh, M. M. Kumar, C. R. Raj and D. Pradhan, Bifunctional Catalytic Activity of Solvothermally Synthesized CeO_2 Nanosphere/NiO Nanoflake Nanocomposites, *ACS Appl. Energy Mater.*, 2022, **5**(5), 5666–5679, DOI: 10.1021/acsaem.1c04036.

54 K. Karthick, S. Subhashini, R. Kumar, S. S. Markandaraj, M. M. Teepikha and S. Kundu, Cubic Nanostructures of Nickel-Cobalt Carbonate Hydroxide Hydrate as a High-Performance Oxygen Evolution Reaction Electrocatalyst in Alkaline and Near-Neutral Media, *Inorg. Chem.*, 2020, **59**(22), 16690–16702, DOI: 10.1021/acs.inorgchem.0c02680.

55 X. Cao, Y. Liu, Y. Zhong, L. Cui, A. Zhang, J. M. Razal, W. Yang and J. Liu, Flexible Coaxial Fiber-Shaped Asymmetric Supercapacitors Based on Manganese, Nickel Co-Substituted Cobalt Carbonate Hydroxides, *J. Mater. Chem. A*, 2020, **8**(4), 1837–1848, DOI: 10.1039/c9ta11942f.

56 S. Kandula, K. R. Shrestha, G. Rajeshkhanna, N. H. Kim and J. H. Lee, Kirkendall Growth and Ostwald Ripening Induced Hierarchical Morphology of Ni-Co LDH/$MMoS_x$(M = Co, Ni, and Zn) Heteronanostructures as Advanced Electrode Materials for Asymmetric Solid-State Supercapacitors, *ACS Appl. Mater. Interfaces*, 2019, **11**(12), 11555–11567, DOI: 10.1021/acsami.9b02978.

57 Y. Zhao, X. He, R. Chen, Q. Liu, J. Liu, J. Yu, J. Li, H. Zhang, H. Dong, M. Zhang and J. Wang, A Flexible All-Solid-State Asymmetric Supercapacitors Based on Hierarchical Carbon Cloth@$CoMoO_4$@NiCo Layered Double Hydroxide Core–Shell Heterostructures, *Chem. Eng. J.*, 2018, **352**, 29–38, DOI: 10.1016/j.cej.2018.06.181.

58 C. Li, W. Yang, W. He, X. Zhang and J. Zhu, Multifunctional Surfactants for Synthesizing High-Performance Energy Storage Materials, *Energy Storage Mater.*, 2021, **43**, 1–19, DOI: 10.1016/j.ensm.2021.08.033.

59 P. Kumar, M. Arumugam, G. Maia, S. Praserthdam and P. Praserthdam, Double Role of CTAB as a Surfactant and Carbon Source in Ni-Mo_2C/GA Composite: As a Highly Active Electrocatalyst for Hydrogen Evolution Reaction, *Electrochim. Acta*, 2023, **441**, 141861, DOI: 10.1016/j.electacta.2023.141861.

60 P. W. Yuan, S. H. Guo, S. Q. Gao, J. Wang, W. Q. Chen, M. Li, K. Y. Ma, N. Wang, F. Liu and J. P. Cheng, Influence of Ni/Cu Ratio in Nickel Copper Carbonate Hydroxide on the

Phase and Electrochemical Properties, *J. Alloys Compd.*, 2019, **780**, 147–155, DOI: **10.1016/j.jallcom.2018.11.334**.

61 Q. Liu, Y. Chen, J. Ma, X. Xiong, X. Zeng and H. Qian, Novel Electrochemical Deposition of $Co(CO_3)_{0.5}(OH)\cdot 0.11H_2O$ Nano-Needles with Folded Umbrella-like Architecture onto Nickel Foam for Supercapacitors, *Surf. Coat. Technol.*, 2021, **421**, 127452, DOI: **10.1016/j.surfcoat.2021.127452**.

62 M. Zhang, X. Liu, M. Ma, G. Ni, Z. Sun, J. Liu and Y. Wu, 3D Hierarchical Urchin-Like $Ni_{0.3}Co_{0.6}Cu_{0.1}(CO_3)_{0.5}(OH)$ Microspheres for Supercapacitors with High Specific Capacitance, *Energy Fuels*, 2021, **35**(24), 20358–20366, DOI: **10.1021/acs.energyfuels.1c03299**.

63 R. Ramachandran, Y. Lan, Z. X. Xu and F. Wang, Construction of NiCo-Layered Double Hydroxide Microspheres from Ni-MOFs for High-Performance Asymmetric Supercapacitors, *ACS Appl. Energy Mater.*, 2020, **3**(7), 6633–6643, DOI: **10.1021/acsaem.0c00790**.

64 T. Q. Nguyen and C. Breitkopf, Determination of Diffusion Coefficients Using Impedance Spectroscopy Data, *J. Electrochem. Soc.*, 2018, **165**(14), E826–E831, DOI: **10.1149/2.1151814jes**.

65 F. Wan, L. Zhang, X. Dai, X. Wang, Z. Niu and J. Chen, Aqueous Rechargeable Zinc/Sodium Vanadate Batteries with Enhanced Performance from Simultaneous Insertion of Dual Carriers, *Nat. Commun.*, 2018, **9**(1), 1656, DOI: **10.1038/s41467-018-04060-8**.

66 J. Liu, J. Wang, C. Xu, H. Jiang, C. Li, L. Zhang, J. Lin and Z. X. Shen, Advanced Energy Storage Devices: Basic Principles, Analytical Methods, and Rational Materials Design, *Adv. Sci.*, 2018, **5**(1), 1700322, DOI: **10.1002/advs.201700322**.

67 R. Kumar and M. Bag, Quantifying Capacitive and Diffusion-Controlled Charge Storage from 3D Bulk to 2D Layered Halide Perovskite-Based Porous Electrodes for Efficient Supercapacitor Applications, *J. Phys. Chem. C*, 2021, **125**(31), 16946–16954, DOI: **10.1021/acs.jpcc.1c05493**.

68 K. Brezesinski, J. Wang, J. Haetge, C. Reitz, S. O. Steinmueller, S. H. Tolbert, B. M. Smarsly, B. Dunn and T. Brezesinski, Pseudocapacitive Contributions to Charge Storage in Highly Ordered Mesoporous Group v Transition Metal Oxides with Iso-Oriented Layered Nanocrystalline Domains, *J. Am. Chem. Soc.*, 2010, **132**(20), 6982–6990, DOI: **10.1021/ja9106385**.

69 S. G. Krishnan, M. Harilal, B. Pal, I. I. Misnon, C. Karuppiah, C. C. Yang and R. Jose, Improving the Symmetry of Asymmetric Supercapacitors Using Battery-Type Positive Electrodes and Activated Carbon Negative Electrodes by Mass and Charge Balance, *J. Electroanal. Chem.*, 2017, **805**, 126–132, DOI: **10.1016/j.jelechem.2017.10.029**.